

RESEARCH ARTICLE

# Effects of X-ray pre-ablation on the implosion process for double-cone ignition

Bihao Xu<sup>1</sup>, Xiaohu Yang<sup>1</sup>, Ze Li<sup>1</sup>, Bo Zeng<sup>1</sup>, Zehao Chen<sup>1</sup>, Lingrui Li<sup>1</sup>, Ye Cui<sup>1</sup>, Guobo Zhang<sup>1</sup>, Yanyun Ma<sup>2,3</sup>, and Jie Zhang<sup>3,4</sup>

<sup>1</sup>College of Science, National University of Defense Technology, Changsha, China

<sup>2</sup>College of Advanced Interdisciplinary Studies, National University of Defense Technology, Changsha, China

<sup>3</sup>Collaborative Innovation Center of IFSA, Shanghai Jiao Tong University, Shanghai, China

<sup>4</sup>Key Laboratory for Laser Plasmas and School of Physics and Astronomy, Shanghai Jiao Tong University, Shanghai, China

(Received 2 December 2024; revised 30 December 2024; accepted 14 January 2025)

## Abstract

The double-cone ignition scheme is a promising novel ignition method, which is expected to greatly save the driver energy and enhance the robustness of the implosion process. In this paper, ablation of the inner surface of the cone by the hard X-ray from coronal Au plasma is studied via radiation hydrodynamics simulations. It is found that the X-ray ablation of the inner wall will form strong pre-plasma, which will significantly affect the implosion process and cause the Au plasma to mix with the fuel, leading to ignition failure. The radiation and pre-ablation intensities in the system are estimated, and the evolutions of areal density, ion temperature and the distribution of Au ions are analysed. In addition, the mixing of Au in CH at collision is quantified. Then, a scheme to reduce the X-ray pre-ablation by replacing the gold cone with a tungsten cone is proposed, showing that it is effective in reducing high-Z mixing and improving collision results.

**Keywords:** double-cone ignition; high-Z mixing; implosion compression; radiation pre-ablation

## 1. Introduction

The concept of laser fusion has been proposed<sup>[1]</sup> for over six decades, during which several potential driving and ignition schemes<sup>[2–5]</sup> have been put forth. Nevertheless, it was not until recently that a breakthrough<sup>[6–9]</sup> was finally achieved at the National Ignition Facility (NIF) in the United States. The fundamental challenge associated with laser fusion can be attributed to two key factors: the limited laser driver energy and the low-energy coupling efficiency from the laser to the fuel. The upper limit of compression for the target is not high, while laser–plasma<sup>[10,11]</sup> and hydrodynamic instabilities<sup>[12,13]</sup> further reduce the implosion symmetry and hydrodynamic efficiency, thereby making it challenging for the areal density and temperature of the fuel to reach the ignition threshold. Presently, the NIF's laser facilities and experimental results

occupy a leading position in this area. Nevertheless, the achievement of high-gain fusion remains a significant challenge, underscoring the necessity for continued exploration of alternative laser fusion schemes. The double-cone ignition (DCI) scheme<sup>[14]</sup> represents a promising new approach to laser fusion, combining the advantages of conventional ignition methods while reducing the instability during implosion and the demand for driver energy<sup>[15]</sup>. In the DCI scheme, a spherical fuel shell is positioned within two oppositely placed open-tip gold cones. Nanosecond lasers are applied to perform quasi-isentropic compression and implosion acceleration on the target. The fuel is ejected at high speed along the axis of the cones from the cone tip under the constraint of the gold cones, colliding to achieve a significant increase in density and temperature. Ultimately, the laser-generated MeV electron beams heat the fuel to the ignition temperature, thereby completing the fusion process.

The DCI team has conducted comprehensive research on the optimization of driving lasers<sup>[16,17]</sup>, hydrodynamic instabilities<sup>[18–21]</sup>, plasma collision<sup>[15,22,23]</sup> and fast heating<sup>[24–27]</sup>. Nevertheless, there is a paucity of investigation into the impact of cones on the DCI process. The most notable

Correspondence to: X. Yang, College of Science, National University of Defense Technology, Changsha 410073, China. Email: xhyang@nudt.edu.cn; Y. Ma, College of Advanced Interdisciplinary Studies, National University of Defense Technology, Changsha 410073, China. Email: yanyunma@126.com

feature of the DCI scheme is the introduction of two gold cones (shell-in-cone), which serve to confine the fuel and thereby reduce the difficulty of the driving process. However, the interaction between the cones and the fuel is very complex and may have adverse effects on the implosion. For instance, the Kelvin–Helmholtz instability (KHI) between the fuel and the cones could lead to material mixing<sup>[28]</sup>. Furthermore, as the fuel implodes and contracts, part of the gold cones will inevitably be exposed to the direct irradiation of high-power lasers. Laser-produced Au plasma is excited to high ionization states, resulting in the emission of X-rays with an intensity that is significantly higher than that produced by low-Z ablaters, such as CH. The hard component of the Au radiation can penetrate the corona and the low-Z fuel shell, causing preheating and pre-ablation of the inner material, which subsequently results in more complex fluid interactions. The plasma produced by the pre-ablation of the gold cones may result in implosion asymmetry and inadequate compression. In addition, it may lead to the mixing of Au ions into the fuel, which could cool the fuel and hinder the ignition. Similar pre-ablation phenomena have been observed in previous studies<sup>[29–32]</sup>, and corresponding mitigation methods have been proposed. Nevertheless, the DCI configuration and the physical processes involved here are distinct from the former (namely cone-in-shell configuration). Therefore, it is of significant worth to study this phenomenon in depth.

In this paper, the implosion physics of DCI is studied using the radiation hydrodynamics code FLASH<sup>[33,34]</sup>. Firstly, the basic model used in the simulation is introduced. Then, the radiation intensity and the pre-ablation intensity in the system are estimated, and the evolution and distribution of the colliding plasma parameters are analysed in order to describe the main interactions and the influence of the pre-plasma on the implosion shell. Finally, the results for tungsten cones are presented, highlighting the influence of cone material on radiation pre-ablation and collision outcomes.

## 2. Simulation model

The DCI scheme is divided into four sequential stages: quasi-isentropic compression, implosion acceleration, plasma collision and fast electron ignition. This paper uses a radiation hydrodynamics code to undertake numerical simulation studies of the initial three processes. The model used is illustrated in Figure 1(a), which is based on the complete DCI structure but excludes the heating cone necessary for fast ignition, retaining the upper and lower two main gold cones and the spherical target situated within the cones. The implosion of the spherical target is driven by multiple laser beams from both the upper and lower directions. The simplified DCI model is symmetrical in both vertical and horizontal directions, as well as exhibiting cylindrical symmetry. Accordingly, in numerical simulations,

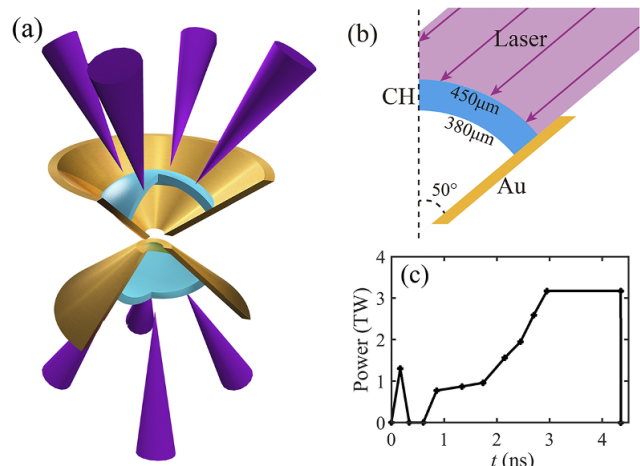


**Figure 1.** Schematic of the setup. (a) Three-dimensional view. (b) Structure of the target. (c) Laser power versus time (loaded onto the target in one cone).

two-dimensional (2D) cylindrical coordinates are employed, with only half of a cone being calculated. By applying symmetric boundary conditions to the left and bottom boundaries of the simulation region, it is possible to restore the complete double cones. The laser pulse shape and target configuration applied in this study are optimized using a random walk and Bayesian algorithm<sup>[35,36]</sup>, based on the nanosecond laser facility to be built at the Shanghai Institute of Optics and Fine Mechanics. As illustrated in Figure 1(b), the distance between the two cone tips is 140 μm, the semi-cone angle is 50°, the inner radius of the target is 380 μm and the thickness is 70 μm. Instead of DT, CH is used as the target, in accordance with the parameters of the current experiments. The laser pulse shape is illustrated in Figure 1(c). The wavelength of the laser is 351 nm, and the light path is parallel to the cone wall. The laser spot radius is 225 μm, which allows for coverage of the whole target without direct irradiation of the cone in the early stages. The radiation hydrodynamics code employs a three-temperature (3T) model, and the radiation unit is based on the diffusion approximation with 20 groups. The equation of state (EOS) employed within the simulation is derived from the FEOS package<sup>[37]</sup>, and the Rosseland and Planck mean opacities are calculated using the non-local thermodynamic equilibrium atomic physics model known as SNOP<sup>[38]</sup>. These EOS and opacity parameters are tabulated as functions of density and electron temperature, and subsequently integrated into the radiation hydrodynamic equations via interpolation.

## 3. Results and discussion

The simulation was carried out according to the parameters shown in Figure 1, and the density evolution throughout the entire process is presented in Figure 2. At approximately 1.8 ns, the shock wave penetrates through the inner surface of the fuel shell, resulting in the entire shell acquiring a radial

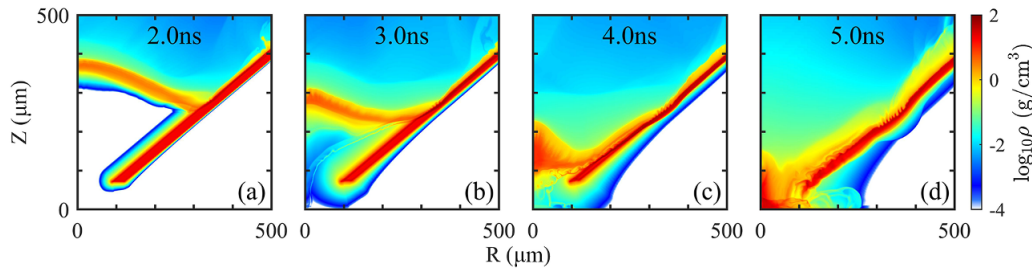


**Figure 2.** Density evolution of the implosion and collision.

acceleration. Simultaneously, a rarefaction wave that propagates outward is reflected, causing the inner surface of the CH to be torn apart and generating low-density pre-plasma. Given that the inner cavity of the gold cone is essentially a vacuum, the rarefaction wave is capable of accelerating the CH pre-plasma to many times the velocity of the main shell. At 3 ns, the CH pre-plasma occupies approximately half of the inner cavity, with the remaining space in the cavity filled with low-density Au pre-plasma. The CH pre-plasma and Au pre-plasma collectively constitute the implosion precursor, colliding at the origin of the simulation domain at approximately 3.5 ns. This occurs approximately 1 ns prior to the collision of the main shell. Furthermore, the symmetry of the main shell is influenced by the presence of the cone and the Au pre-plasma. At 2.0 ns, the main shell maintains a spherical shape of satisfactory quality. However, by 3.0 ns, the implosion velocity of the shell adjacent to the cone is markedly slower than that of the shell near the axis due to the obstruction of the Au pre-plasma. By 4 ns, the distortion of the main shell is more pronounced, which will unavoidably impact the collision process and compression results.

From the early density distribution at 2.0 ns (Figure 2(a)), it can be seen that the low-density Au plasma on the inner surface of the cone is uniformly produced. This observation rules out the possibility that the cause is the shock wave from the main shell, as the propagation speed of the shock is insufficient to generate plasma on the entire cone simultaneously. In addition, the driving laser configuration in the simulation does not enter the cavity from the simulation boundary or cone tip, thereby ensuring that the Au pre-plasma is not produced by laser ablation. It can thus be surmised that the Au pre-plasma is associated with radiation ablation.

### 3.1. Radiation preheating and pre-ablation

Given that the target is 70  $\mu\text{m}$  thick CH, it can be inferred that only the hard X-rays, which may be generated by the gold cone, can penetrate the target and reach the inner cavity. In another simulation, the gold cone is defined as a rigid body in order to facilitate a more accurate comparison between the radiation produced by the gold cone and that produced by pure CH. In the FLASH code, a rigid body is defined as a static solid that does not engage in any

physical interactions or fluid calculations, with reflecting boundary conditions applied to its surfaces. To ensure accuracy and stability, adaptive mesh refinement, lower-order reconstruction methods and a reduced Courant–Friedrichs–Lewy (CFL) number are employed in the vicinity of the rigid body. Figure 3 presents the temperature distributions and radiation spectra at different positions. As illustrated in the figure, the temperature distribution in the coronal region is similar between the two simulations, whereas that in the inner cavity exhibits notable differences. The electron temperature within the inner cavity of the rigid case is relatively low and evenly distributed, with a value of approximately 10 eV. In contrast, the inner temperature of the normal case is considerably higher and more complex, with the overall electron temperature exceeding 40 eV and locally reaching up to 90 eV. This indicates the potential for the existence of sophisticated fluid processes.

The radiation temperature distribution in both the corona and the inner cavity is relatively uniform, due to the large mean free path of X-rays in these low-density regions. In order to estimate the radiation intensity in the corona and the cavity, sampling is performed at positions that are distant from the axis and the cone wall, as illustrated in Figure 3. It is evident that the interior radiation temperature of the normal case is considerably higher than that of the rigid case. As illustrated in Figures 3(b) and 3(d), this phenomenon can be attributed to the presence of gold M-band radiation, with a photon energy exceeding 2 keV. Once gold has been designated as a rigid body, only CH participates in the radiation process. At high temperatures, CH is fully ionized, with the emission spectra closely approximating that of a blackbody. However, when gold is taken into account, there is a notable non-equilibrium radiation component (2.4–2.8 keV in the curve, which corresponds to gold M-band radiation), resulting in a shift in the spectra as a whole towards the high-energy direction compared to the blackbody spectra. As illustrated in Figure 3(b), the corona temperature of the normal case is 112 eV, with a proportion of hard X-rays above 2 keV at 19.7% (of which the M-band is 15%). Figure 3(d) indicates that the corona temperature of the rigid case is 100 eV, with a proportion of hard X-rays of 0.3%. Using the relationship  $S \sim \sigma T^4$ , it can be estimated that the hard X-ray energy flux of the former is 103 times that of the latter.

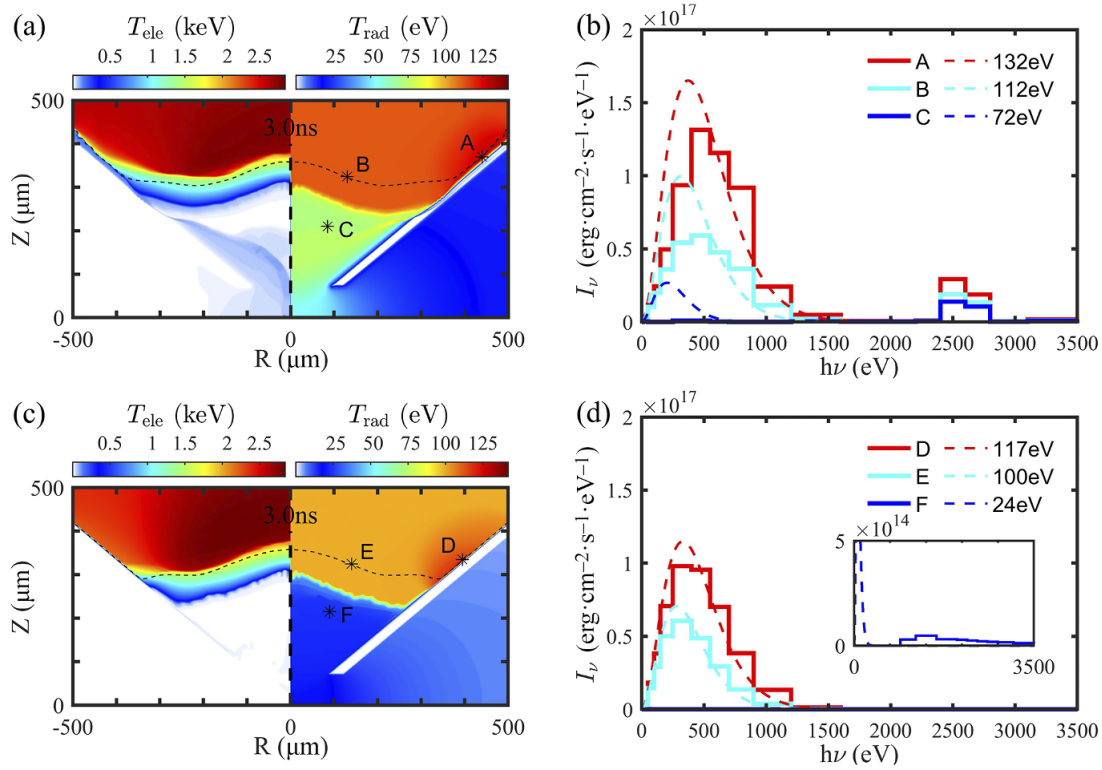


**Figure 3.** Temperature distribution and radiation spectra at different positions at 3 ns, (a), (b) for the normal case and (c), (d) for the rigid case. The dashed lines in (a) and (c) mark the positions of the critical surface. The solid and dashed lines in (b) and (d) represent the group spectra of each sampling point and the blackbody spectra at the equivalent radiation temperatures, respectively.

The mean free path of hard X-rays in the fuel shell layer is significantly greater than that of soft X-rays, resulting in hard X-rays dominating the inner cavity. Consequently, the total radiation flux intensity in the inner cavity of the former is  $(72/24)^4 = 81$  times that of the latter.

Figure 4(a) shows the evolution of the mean radiation temperature in the corona and the inner cavity before the collision. Since the main shell reaches the cone tip at 4 ns, the inner temperature is only counted up to 4 ns. It is evident that the evolution of the radiation temperature in the corona is roughly correlated with the changes in the laser pulse shape. In addition, the inner temperature undergoes a simultaneous change due to the preheating by hard X-rays from the corona. However, after 3 ns, the inner temperature exhibits a different trend, continuing to rise, which suggests that X-ray preheating is no longer the dominant factor. Combined with Figure 2, it can be seen that the cavity is filled with pre-plasma, and the fluid processes inside the cavity begin to become important after 3 ns. The kinetic energy of the pre-plasma is partially converted into internal energy, leading to a continuous increase in temperature. For the rigid case, due to the lack of hard X-rays, the preheating inside the cavity is very weak, and the temperature increases slowly.

Hard X-rays can easily penetrate the target shell, but their mean free path in solid gold is very short, causing subsonic ablation on the inner surface of the gold cone. When the radiation driving temperature changes over time, the ablated

mass of gold can be written as a function of the driving temperature  $T_s(t)$  and time<sup>[39]</sup>:

$$m(t) = m_0 T_s(t)^{1.914} t^{0.5156}, \quad (1)$$

where  $T_s(t) = T_0 t^k = T_0 t^{q_0/5.5}$ . The units for  $T_0$  and  $t$  are keV and ns, respectively. By fitting the curves in the Ref. [39], the relationship between  $m_0$  and  $q_0$  can be obtained as follows:

$$m_0 = e^{-(8.194q_0 + 23.21)/(q_0 + 3.35)} \text{ (g/cm}^2\text{)}. \quad (2)$$

In Figure 4(a), the variation trend of the inner temperature can be approximately regarded as proportional to time, that is, the time index  $k$  of  $T_s$  is 1, and the ablated mass can be written as follows:

$$m(t) = 0.4485 T_0^{1.914} t^{2.4296} \text{ (mg/cm}^2\text{)}. \quad (3)$$

It can be observed that the ablated mass is related to  $T_0$ , which represents the slope of  $T_s$ . The temperature slope of the normal case in Figure 4(a) is approximately three times that of the rigid case. It can therefore be inferred that the final ablated mass of the former is roughly 10 times that of the latter. The evolution of the ablated mass in Figure 4(b) was obtained through one-dimensional (1D) simulation, using the inner radiation temperature as the driver for the ablation of solid gold. The final ablated mass of the normal case was



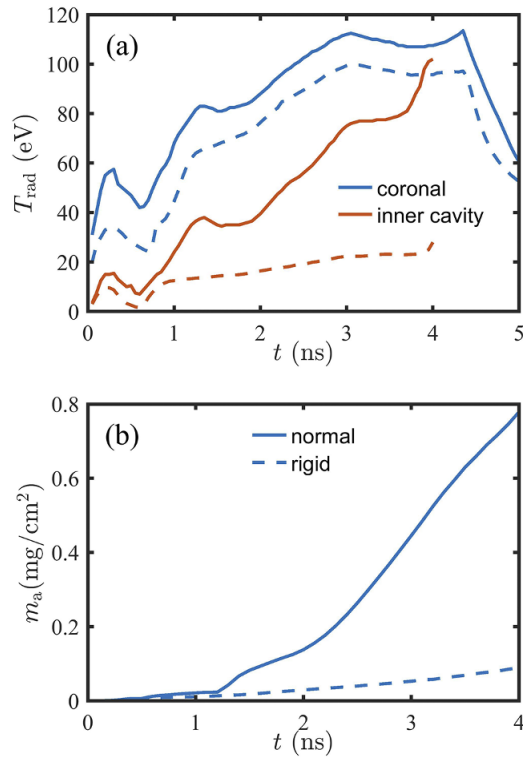


**Figure 4.** (a) The average radiation temperature in the corona and inner cavity versus time. (b) The ablated mass of a solid gold slab versus time, with the inner cavity radiation temperature serving as the driver. The solid and dashed lines represent the normal case and the rigid case, respectively.

found to be  $0.78 \text{ mg}/\text{cm}^2$ , while that of the rigid case was  $0.09 \text{ mg}/\text{cm}^2$ , representing a final mass 8.7 times greater than that of the latter. This result is in good agreement with the theoretical estimate.

During the implosion process, the radius of the target continuously decreases, resulting in a reduction in the inner surface area of the cone. On the basis of the ablation rate and the change in area, it can be numerically calculated that the total mass of gold ablated inside the single cone is approximately  $1.1 \text{ }\mu\text{g}$ , which has reached 3.7% of the initial mass of CH ( $30 \text{ }\mu\text{g}$ ). The ablated mass is  $0.14 \text{ }\mu\text{g}$  when the driver temperature is taken from the rigid case, which is 13.5% of the former. The Au plasma is propelled towards the cone tip under the compression of the imploding CH. Although some of the Au plasma moves laterally after exiting the cone tip and does not enter the centre of the colliding plasma, it is evident that this still increases the risk of material mixing. The mixing of high-Z into low-Z elements results in a notable enhancement of bremsstrahlung power, which causes a reduction in the temperature of the colliding plasma. This is an unfavourable condition for ignition. In accordance with the DCI scheme concept, the fuel is DT, with an electron temperature of approximately 10 keV at ignition. At this temperature, the average ionization of Au is above 60, while that of DT is 1. The bremsstrahlung power

is proportional to the square of the effective ionization<sup>[40]</sup>, that is

$$P_{\text{br}} \propto n_e n_i Z_{\text{eff}}^2 T_e^{1/2}. \quad (4)$$

If every 10,000 DT ions are mixed with 1 Au ion (mass fraction 0.78%), the effective ionization and bremsstrahlung power will be 1.35 and 1.82 times that of pure DT, respectively. This demonstrates that even a minor quantity of high-Z mixing can result in a considerable enhancement in bremsstrahlung losses.

### 3.2. Impact of Au pre-plasma on implosion and material mixing

The large free paths of M-band radiation in the CH and the thin gold plasma result in a uniform radiation temperature distribution in the cavity, which is conducive to the formation of isothermal rarefied waves. The input energy of the radiation field serves to offset the internal energy attenuation that is caused by the expansion of the plasma, thereby ensuring the continuous acceleration of the plasma. As previously stated, two distinct types of plasma are present within the cavity: a CH pre-plasma formed by shock and a gold pre-plasma formed by radiation ablation. The simulations indicate that at 3 ns, the tail velocities of the CH and gold rarefaction waves are approximately 300 and 100 km/s, respectively. The former moves along the radial direction, while the latter moves along the normal direction of the conical wall. Upon encountering each other, these two types of plasma engage in a complex fluid interaction.

Figure 5 illustrates the density and pressure distributions at 3.2 ns, with the range of gold marked by dashed lines. At this point, the inner cavity is already filled with low-density plasma, with the cone tip area almost blocked by Au plasma. In contrast, when the radiation module of the FLASH software is disabled, there is no observable expansion of the gold cone within the inner cavity, and it remains in a fixed position. The contour line of the Au plasma in the inner cavity indicates that the Au and CH plasmas meet and collide, resulting in a simultaneous increase in density and pressure near the interface of nearly two orders of magnitude compared to the non-radiation case. At the interface between the Au plasma and the CH plasma, the density reaches  $0.1\text{--}1 \text{ g}/\text{cm}^3$ . This interfacial discontinuity and unevenness promote hydrodynamic instability, potentially leading to material mixing. Furthermore, plasma collision also generates shock waves that propagate towards the fuel shell, increasing the interior pressure to several Mbar, corresponding to the light blue area near the dashed line in Figure 5(b). This creates resistance to the radial motion of the implosion shell, resulting in additional implosion kinetic energy loss and a reduction in implosion compression

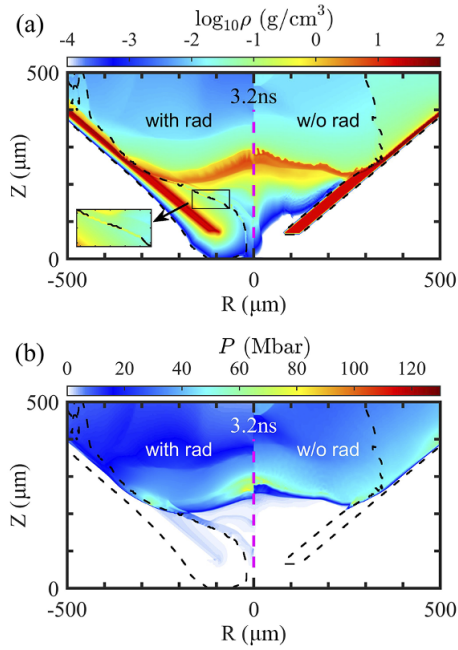


**Figure 5.** Comparison of (a) density and (b) pressure distributions at 3.2 ns, with the radiation module enabled (left, the normal case) and disabled (right, the non-radiation case). The dashed lines indicate the edges of the Au distribution.

efficiency. Conversely, when the radiation module is disabled, the pressure in the cone cavity is low, eliminating this issue.

In order to gain insight into the details of the implosion and collision, the evolution of the areal density in different directions over time is presented in Figures 6(a) and 6(b), which is calculated as follows:

$$\rho R = \sum_i \rho_i \Delta x_i \quad (-100 \mu\text{m} < x_i < 100 \mu\text{m}). \quad (5)$$

The two sets of results show similar areal density curves. The peak areal density of both cases is achieved at approximately 5 ns, which is also considered to be the time of peak compression. At this point, the average areal density is approximately  $0.26 \text{ g/cm}^2$ . The highest values of areal density distribution are observed along the axial direction, which is consistent with the initial configuration of the double cone. However, the assumption of DCI is that the ideal colliding plasma should be spherically distributed, with equal areal density in all directions, whereas the current results demonstrate a discrepancy of up to 30% between different directions. Furthermore, the axial areal density attains its maximum value significantly later than in other directions, as illustrated in Figures 6(a) and 6(b), indicating that the initial parameters of the target and the laser pulse require further optimization. In contrast to the areal density, the divergence between the two sets of temperature curves is considerably more pronounced. Two principal discrepancies

can be identified. The first is that the pre-plasma in the normal case collides at 4.2 ns, resulting in an observable increase in temperature, whereas in the non-radiation case, it occurs later (at 4.6 ns). The second is that the temperature at peak compression is lower in the normal case (300 eV) than in the non-radiation case (400 eV) due to bremsstrahlung losses.

Another notable consequence of radiation on the plasma is the mixing of Au ions. Figures 6(c) and 6(d) illustrate the density distribution and Au ion distribution at peak compression. These figures show that in the absence of radiation, gold is distributed at the periphery of the collision zone ( $> 50 \mu\text{m}$ ), whereas with radiation, a greater number of Au ions are mixed into the centre of the collision plasma. In order to provide a visual representation of the changes in Au concentration in different regions, the average mass fraction of Au in different radial ranges is statistically analysed as follows:

$$\bar{f}_{\text{Au}} = \frac{\sum f_i \rho_i \Delta V_i}{\sum \rho_i \Delta V_i} \quad (R_1 < |\vec{r}_i| < R_2), \quad (6)$$

where  $\Delta V_i = 2\pi |\vec{r}_i| \Delta x_i \Delta y_i$  is the volume of the  $i$ th grid. The statistical results are presented in Figures 6(e) and 6(f). Figure 6(e) illustrates that the Au concentration in the normal case reaches its first peak at approximately 3 ns, as evidenced in Figure 2(b), where the Au plasma effectively obstructs the entire cone tip and fills the collision region. As the CH pre-plasma gradually approaches the collision point, Au ions are partially propelled away from the collision point by the CH, resulting in a rapid decrease in the proportion of Au ions within a radius of  $20 \mu\text{m}$ . After 4 ns, the CH main shell is ejected from the cone tip, by which Au ions situated exceeding  $40 \mu\text{m}$  are extruded by CH and subsequently re-enter the core, ultimately remaining within the collision centre region. Concurrently, the accumulation of CH results in a dilution of the Au concentration. The average mass fraction of Au in the central  $10 \mu\text{m}$  is 0.21% at peak compression, with a value of 0.13% in the range of  $10\text{--}20 \mu\text{m}$ . The local maximum value of the Au mass fraction exceeds 5%, which is equivalent to a number fraction of 0.2%. This results in the bremsstrahlung power becoming 1.46 times that of pure CH at the ignition temperature (10 keV). Replacing CH with DT would result in a bremsstrahlung power 3.27 times that of pure DT, which would be fatal for ignition. Figures 6(d) and 6(f) illustrate that the non-radiation case exhibits a negligible presence of Au ions within  $40 \mu\text{m}$  from the collision centre, while a considerable number of Au ions are present in the region extending beyond  $60 \mu\text{m}$ . This indicates that the Au mixing observed in the periphery of the collision centre in the normal case (Figure 6(c)) may not be directly related to radiation and is more likely caused by fluid interactions between the implosion shell and the gold cone, such as KHI<sup>[41]</sup>. This suggests that the interaction between

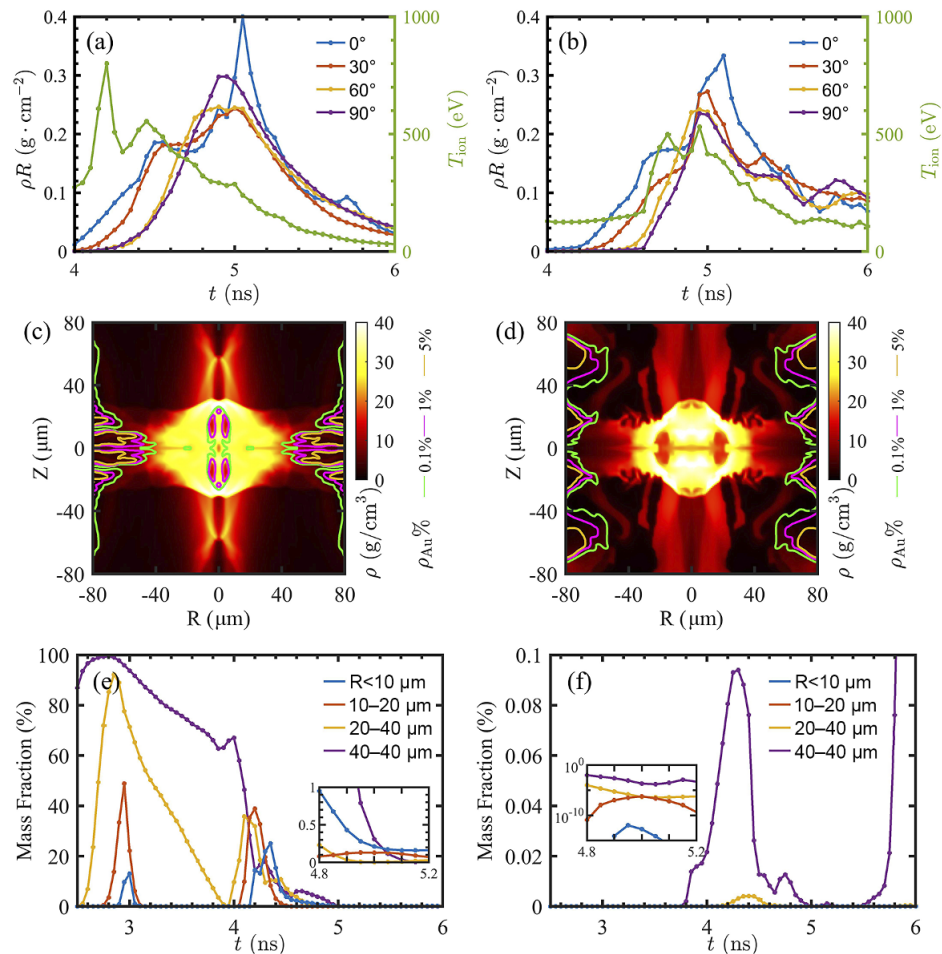


**Figure 6.** (a), (b) Areal density and peak ion temperature versus time, where the areal density is calculated within  $\pm 100$   $\mu\text{m}$  from the collision centre and the angle is with respect to the  $+y$  direction. (c), (d) Density and Au distribution at peak compression. (e), (f) Au ion mass fraction in different radius ranges versus time. (a), (c), (e) Radiation module enabled. (b), (d), (f) Radiation module disabled.

the implosion shell and the gold cone is highly complex and requires further investigation.

### 3.3. Results of the tungsten cone

The presence of gold radiation has a considerable influence on implosion and material mixing. Therefore, it is essential to prevent the transportation of radiation into the inner cavity when optimizing the DCI design. There are two principal methods of radiation suppression: the first is the utilization of a high-Z coating or doping to create a shielding layer for the fuel, thereby reducing the penetration depth of radiation; the second is the alteration of the radiation source composition, thus reducing the proportion of the hard component of the radiation spectra. The former method requires a redesign of both the driving laser and the target, which is complex and requires a substantial workload. Therefore, the second method was selected. In the context of DCI, it is recommended that the cones be constructed from materials with high density and high impedance to constrain the trajectory

of the imploding fuel effectively. Tungsten represents a potential alternative material for the cone. Tungsten has a density comparable to that of gold but with a higher acoustic impedance, which provides superior compressive and impact resistance to that of gold. In addition to the differences in mechanical properties, there are also some differences in radiation performance between W and Au<sup>[42]</sup>. Specifically, the laser-to-X-ray conversion rate of W is slightly lower than that of Au, indicating that under the same laser ablation conditions, the radiation intensity of W is lower than that of Au. Based on this, simulations were conducted with tungsten cones to preliminarily verify the above ideas, and the simulation results are shown in Figure 7.

Figures 7(a) and 7(b) illustrate that the radiation temperature and the hardness of the spectra are both lower than those of the gold cone. The proportion of photons with energy above 2 keV is 6.9%, which is equivalent to a reduction in the hard X-ray flux of 70% in comparison to the latter. As the inner cavity temperature is consistently approximately 20 eV lower than that of the gold cone, it can be concluded that the radiative pre-ablation is weaker. The numerical

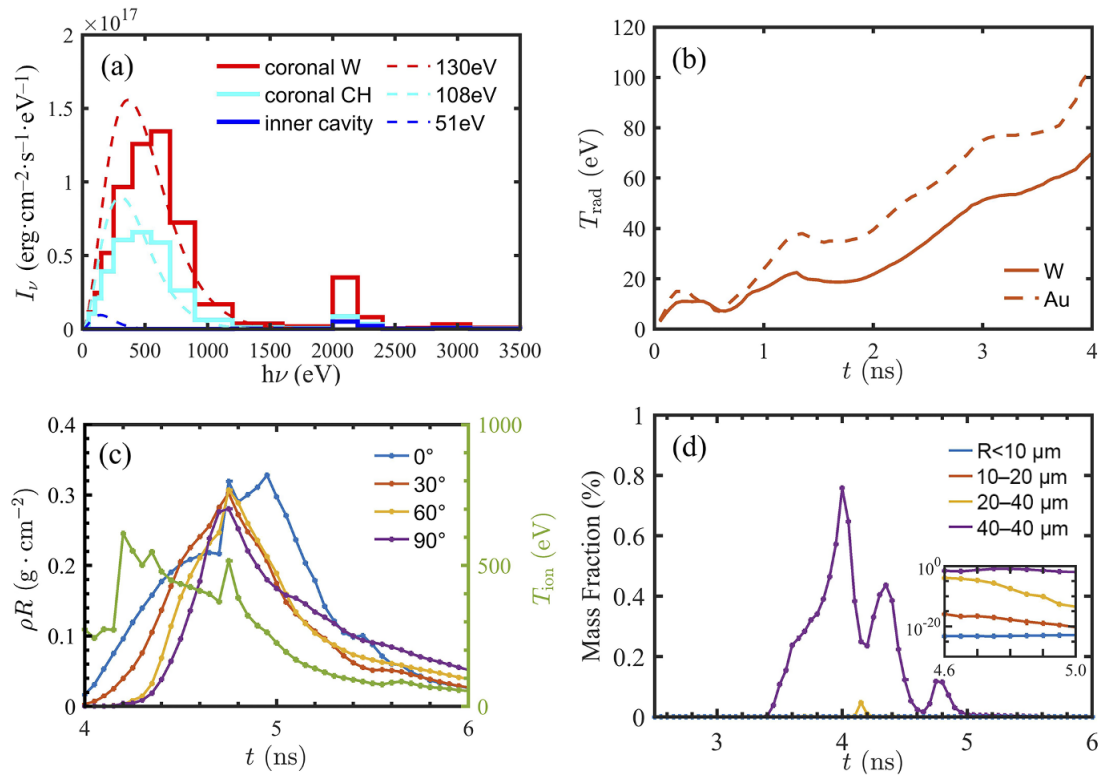


**Figure 7.** Simulation results using a tungsten cone. (a) Radiation spectra at different positions at  $t = 3$  ns. (b) Interior radiation temperature versus time (compared with a gold cone). (c) Areal density and peak ion temperature versus time. (d) W ion mass fraction in different radius ranges versus time.

simulations indicate that the ablated mass of tungsten at 4 ns is only 50% of that of gold in Figure 4(b), which is highly beneficial to reducing fluid interactions and material mixing. Furthermore, the deployment of tungsten cones has been observed to exert a slight enhancement in the collision effect, as illustrated in Figure 7(c). At peak compression (4.75 ns), areal density in all directions is nearly equivalent, indicating that the distribution of the colliding plasma is more spherical. The average areal density is approximately 0.3 g/cm<sup>2</sup>, which is 0.04 g/cm<sup>2</sup> higher than that of the gold cone case, representing a 15% increase. The evolution trend of the peak temperature is similar to that of the gold cone, while the plasma temperature at peak compression is 200 eV higher. The evolution of the W ion mass fraction, as illustrated in Figure 7(d), reveals that W ions never enter the region within 20  $\mu\text{m}$  from the collision centre. This is attributable to the lower pre-ablation intensity, which results in a smaller volume of W pre-plasma. The mass fraction of W ions throughout the process is negligible within a radius of 40  $\mu\text{m}$ , specifically with a value below  $10^{-7}$  at peak compression, which is a significantly more favourable result.

Note that the simulation parameters were configured based on the capabilities of current SG-II upgrade facilities, with a particular emphasis on evaluating the effects of radiation pre-ablation on the implosion and compression of the DCI scheme. However, there remains a notable challenge in achieving ignition. Prior studies have demonstrated that for

DT plasma, the penetration range of 1-MeV electrons is approximately 0.6 g/cm<sup>2</sup><sup>[43–46]</sup>, whereas our current work achieves only 0.3 g/cm<sup>2</sup>, which is marginally adequate for the areal density required for alpha particle energy deposition (0.3–0.4 g/cm<sup>2</sup>)<sup>[41]</sup>, but insufficient for ignition electrons. The DCI team is currently constructing a new laser facility capable of providing  $2 \times 80$  kJ of drive energy, which is 10-fold that of the laser in our simulation. With these enhanced laser parameters, an optimized design with an areal density of 1.3 g/cm<sup>2</sup> has been proposed<sup>[47]</sup>, which makes high gain possible for the DCI scheme.

#### 4. Conclusion

The influence of radiation pre-ablation on plasma formation and implosion processes is investigated by using the radiation hydrodynamics simulations, as well as the collision outcome. It is found that the radiation temperature of the inner cavity increases by tens of eV due to the gold M-band radiation, and that the total ablated mass of the gold cone is approximately 4.3% of the initial mass of the fuel. This results in the closure of the cone tip and a complex fluid interaction within the inner cavity. The radiation increases the density and pressure of the pre-plasma in the inner cavity by approximately two orders of magnitude, which affects the subsequent compression and collision. An analysis of the parameters of the colliding plasma reveals that the areal



density distribution is not uniform and that the temperature decreases due to bremsstrahlung. The local doping ratio of gold at peak compression is up to 5%, with an average doping ratio of 0.21% in the vicinity of the collision centre. Ultimately, it is proposed that the radiation intensity and pre-ablation intensity can be reduced by modifying the cone material. The results demonstrate that a tungsten cone can effectively reduce the generation of hard X-rays and lower the radiation temperature in the inner cavity. In addition, the areal density distribution and plasma temperature at peak compression exhibit a notable improvement, and the high-Z mixing can be disregarded. Overall, the performance of the tungsten cone is superior to that of the gold cone. The prospective next step would be to further optimize the laser irradiation mode with a view of reducing the direct irradiation of the cone, or adding a radiation shield in the ablation layer with the objective of preventing the transmission of hard X-rays and thereby inhibiting the pre-ablation of radiation in the inner cavity.

### Acknowledgements

This work was supported by the Strategic Priority Research Program of the Chinese Academy of Sciences (Grant Nos. XDA25050200 and XDA25010100), the National Natural Science Foundation of China (Grant Nos. 12175309, 12475252, 12275356 and 12075317) and the Defense Industrial Technology Development Program (Grant No. CKYS2023212807).

### References

1. J. Nuckolls, L. Wood, A. Thiessen, and G. Zimmerman, *Nature* **239**, 139 (1972).
2. J. D. Lindl, *AIP Conf. Proc.* **318**, 635 (1994).
3. J. Lindl, *Phys. Plasmas* **2**, 3933 (1995).
4. M. Tabak, J. Hammer, M. Glinsky, W. Kruer, S. Wilks, J. Woodworth, M. Campbell, M. Perry, and R. Mason, *Phys. Plasmas* **1**, 1626 (1994).
5. R. S. Craxton, K. S. Anderson, T. R. Boehly, V. N. Goncharov, D. R. Harding, J. P. Knauer, R. L. McCrory, P. W. McKenty, D. D. Meyerhofer, J. F. Myatt, A. J. Schmitt, J. D. Sethian, R. W. Short, S. Skupsky, W. Theobald, W. L. Kruer, K. Tanaka, R. Betti, T. J. B. Collins, J. A. Delettrez, S. X. Hu, J. A. Marozas, A. V. Maximov, D. T. Michel, P. B. Radha, S. P. Regan, T. C. Sangster, W. Seka, A. A. Solodov, J. M. Soures, C. Stoeckl, and J. D. Zuegel, *Phys. Plasmas* **22**, 110501 (2015).
6. H. Abu-Shawareb, R. Acree, P. Adams, *et al.* (The Indirect Drive ICF Collaboration), *Phys. Rev. Lett.* **132**, 065102 (2024).
7. O. A. Hurricane, D. A. Callahan, D. T. Casey, A. R. Christopher, A. L. Kritcher, O. L. Landen, S. A. MacLaren, R. Nora, P. K. Patel, J. Ralph, D. Schlossberg, P. T. Springer, C. V. Young, and A. B. Zylstra, *Phys. Rev. Lett.* **132**, 065103 (2024).
8. A. L. Kritcher, A. B. Zylstra, C. R. Weber, O. A. Hurricane, D. A. Callahan, D. S. Clark, L. Divol, D. E. Hinkel, K. Humbird, O. Jones, J. D. Lindl, S. MacLaren, D. J. Strozzi, C. V. Young, A. Allen, B. Bachmann, K. L. Baker, T. Braun, G. Brunton, D. T. Casey, T. Chapman, C. Choate, E. Dewald, J.-M. G. D. Nicola, M. J. Edwards, S. Haan, T. Fehrenbach, M. Hohenberger, E. Kur, B. Kustowski, C. Kong, O. L. Landen, D. Larson, B. J. MacGowan, M. Marinak, M. Millot, A. Nikroo, R. Nora, A. Pak, P. K. Patel, J. E. Ralph, M. Ratledge, M. S. Rubery, D. J. Schlossberg, S. M. Sepke, M. Stadermann, T. I. Suratwala, R. Tommasini, R. Town, B. Woodworth, B. V. Wonterghem, and C. Wild, *Phys. Rev. E* **109**, 025204 (2024).
9. M. S. Rubery, M. D. Rosen, N. Aybar, O. L. Landen, L. Divol, C. V. Young, C. Weber, J. Hammer, J. D. Moody, A. S. Moore, A. L. Kritcher, A. B. Zylstra, O. Hurricane, A. E. Pak, S. MacLaren, G. Zimmerman, J. Harte, and T. Woods, *Phys. Rev. Lett.* **132**, 065104 (2024).
10. B. J. MacGowan, B. B. Afeyan, C. A. Back, R. L. Berger, G. Bonnaud, M. Cassanova, B. I. Cohen, D. E. Desenne, A. G. Dulieu, D. F. DuBois, K. G. Estabrook, J. C. Fernandez, S. H. Glenzer, D. E. Hinkel, T. B. Kaiser, D. H. Kalantar, R. L. Kaufman, R. K. Kirkwood, A. B. Langdon, and W. L. Kruer, *Phys. Plasmas* **3**, 2029 (1996).
11. D. S. Montgomery, *Phys. Plasmas* **23**, 055601 (2016).
12. S. Atzeni and A. Caruso, *Il Nuovo Cimento. B* **80**, 71 (1984).
13. Y. Zhou, T. T. Clark, D. S. Clark, S. G. Glendinning, M. A. Skinner, C. M. Huntington, O. A. Hurricane, A. M. Dimits, and B. A. Remington, *Phys. Plasmas* **26**, 080901 (2019).
14. J. Zhang, W. M. Wang, X. H. Yang, D. Wu, Y. Y. Ma, J. L. Jiao, Z. Zhang, F. Y. Wu, X. H. Yuan, Y. T. Li, and J. Q. Zhu, *Philos. Trans. R. Soc. A Math. Phys. Eng. Sci.* **378**, 20200015 (2020).
15. Z. Zhang, X. H. Yuan, Y. H. Zhang, H. Liu, K. Fang, C. L. Zhang, Z. D. Liu, X. Zhao, Q. L. Dong, G. Y. Liu, Y. Dai, H. C. Gu, Y. T. Li, J. Zheng, J. Y. Zhong, and J. Zhang, *Acta Phys. Sin.* **71**, 155201 (2022).
16. F. Y. Wu, X. H. Yang, Y. Y. Ma, Q. Zhang, Z. Zhang, X. H. Yuan, H. Liu, Z. D. Liu, J. Y. Zhong, J. Zheng, Y. T. Li, and J. Zhang, *High Power Laser Sci. Eng.* **10**, e39 (2022).
17. Y. J. Zhang, W. Fan, X. H. Lu, J. F. Wang, X. C. Wang, Y. L. Zhang, X. Q. Jiang, B. Y. Wang, F. Y. Wu, and W. M. Wang, *Opt. Express* **32**, 39483 (2024).
18. K. Fang, Z. Zhang, Y. T. Li, and J. Zhang, *Acta Phys. Sin.* **71**, 035204 (2022).
19. H. H. Dai, M. H. Xu, H. Y. Guo, Y. J. Li, and J. Zhang, *Chinese Phys. B* **31**, 120401 (2022).
20. Z. Y. Zhu, Y. X. Liu, Y. J. Li, and J. Zhang, *Chinese Phys. B* **31**, 105202 (2022).
21. Z. H. Chen, X. H. Yang, G. B. Zhang, Y. Y. Ma, R. Yan, H. Xu, Z. M. Sheng, F. Q. Shao, and J. Zhang, *Nucl. Fusion* **64**, 126029 (2024).
22. M. Q. Yang, F. Y. Wu, Z. B. Chen, Y. X. Zhang, Y. Chen, J. C. Zhang, Z. F. Chen, Z. F. Fang, R. Ramis, and J. Zhang, *Acta Phys. Sin.* **71**, 225202 (2022).
23. Z. D. Liu, F. Y. Wu, Y. P. Zhang, X. H. Yuan, Z. Zhang, X. Y. Xu, Y. H. Xue, J. S. Tian, J. Y. Zhong, and Z. Jie, *Phys. Plasmas* **31**, 042704 (2024).
24. X. H. Yang, C. Ren, H. Xu, Y. Y. Ma, and F. Q. Shao, *High Power Laser Sci. Eng.* **8**, e11 (2020).
25. X. H. Yang, Z. H. Chen, H. Xu, Y. Y. Ma, G. B. Zhang, D. B. Zou, and F. Q. Shao, *Matter Radiat. Extremes* **8**, 035901 (2023).
26. T. H. Zhang, W. M. Wang, Y. T. Li, and J. Zhang, *Phys. Rev. Lett.* **132**, 065105 (2024).
27. Z. Y. Chen, K. G. Zhao, and Y. J. Li, *Chinese Phys. B* **33**, 115202 (2024).
28. A. Caruso and C. Strangio, *J. Exp. Theor. Phys.* **97**, 948 (2003).
29. R. B. Stephens, S. P. Hatchett, R. E. Turner, K. A. Tanaka, and R. Kodama, *Phys. Rev. Lett.* **91**, 185001 (2003).
30. W. Theobald, A. A. Solodov, C. Stoeckl, K. S. Anderson, R. Betti, T. R. Boehly, R. S. Craxton, J. A. Delettrez, C. Dorner, J. A. Frenje, V. Y. Glebov, H. Habara, K. A. Tanaka, J. P. Knauer, R. Lauck, F. J. Marshall, K. L. Marshall, D. D. Meyerhofer, P.

- M. Nilson, P. K. Patel, H. Chen, T. C. Sangster, W. Seka, N. Sinenian, T. Ma, F. N. Beg, E. Giraldez, and R. B. Stephens, *Phys. Plasmas* **18**, 056305 (2011).
31. H. D. Shay, P. Amendt, D. Clark, D. Ho, M. Key, J. Koning, M. Marinak, D. Strozzi, and M. Tabak, *Phys. Plasmas* **19**, 092706 (2012).
32. K. S. Raman, V. A. Smalyuk, D. T. Casey, S. W. Haan, D. E. Hoover, O. A. Hurricane, J. J. Kroll, A. Nikroo, J. L. Peterson, B. A. Remington, H. F. Robey, D. S. Clark, B. A. Hammel, O. L. Landen, M. M. Marinak, D. H. Munro, K. J. Peterson, and J. Salmonson, *Phys. Plasmas* **21**, 072710 (2014).
33. B. Fryxell, K. Olson, P. Ricker, F. X. Timmes, M. Zingale, D. Q. Lamb, P. MacNeice, R. Rosner, J. W. Truran, and H. Tufo, *Astrophys. J. Suppl. Ser.* **131**, 273 (2000).
34. P. Tzeferacos, M. Fatenejad, N. Flocke, C. Graziani, G. Gregori, D. Q. Lamb, D. Lee, J. Meinecke, A. Scopatz, and K. Weide, *High Energy Density Phys.* **17**, 24 (2015).
35. Z. Li, X. H. Yang, H. Xu, G. B. Zhang, B. Zeng, S. J. Chen, Y. Y. Ma, F. Y. Wu, and J. Zhang, *Phys. Plasmas* **29**, 092705 (2022).
36. Z. Li, Z. Q. Zhao, X. H. Yang, G. B. Zhang, Y. Y. Ma, H. Xu, F. Y. Wu, F. Q. Shao, and J. Zhang, *Plasma Phys. Control. Fusion* **66**, 015010 (2024).
37. S. Faik, A. Tauschwitz, and I. Iosilevskiy, *Comput. Phys. Commun.* **227**, 117 (2018).
38. K. Eidmann, *Laser Particle Beams* **12**, 223 (1994).
39. J. H. Hammer and M. D. Rosen, *Phys. Plasmas* **10**, 1829 (2003).
40. R. J. Gould, *Astrophys. J.* **238**, 1026 (1980).
41. Q. Zhang, F. Y. Wu, X. H. Yang, Y. Y. Ma, Y. Cui, B. F. Jiang, and J. Zhang, *Phys. Plasmas* **31**, 032703 (2024).
42. G. Mishra, K. Ghosh, A. Ray, and N. K. Gupta, *High Energy Density Phys.* **27**, 1 (2018).
43. C. K. Li and R. D. Petrasso, *Phys. Plasmas* **13**, 056314 (2006).
44. A. A. Solodov and R. Betti, *Phys. Plasmas* **15**, 042707 (2008).
45. S. Atzeni, A. Schiavi, and J. R. Davies, *Plasma Phys. Control. Fusion* **51**, 015016 (2009).
46. W. Theobald, A. A. Solodov, C. Stoeckl, K. S. Anderson, F. N. Beg, R. Epstein, G. Fiksel, E. M. Giraldez, V. Y. Glebov, H. Habara, S. Ivancic, L. C. Jarrott, F. J. Marshall, G. McKiernan, H. S. McLean, C. Mileham, P. M. Nilson, P. K. Patel, F. Pérez, T. C. Sangster, J. J. Santos, H. Sawada, A. Shvydky, R. B. Stephens, and M. S. Wei, *Nat. Commun.* **5**, 5785 (2014).
47. H. Y. Song, F. Y. Wu, Z. M. Sheng, and J. Zhang, *Phys. Plasmas* **30**, 092707 (2023).